Available online at www.sciencedirect.com

ScienceDirect

Ceramics International 40 (2014) 2401–2410

CERAMICS INTERNATIONAL

www.elsevier.com/locate/ceramint

Influence of sintering parameters on microstructure and electrical conductivity of $La_{10}Si_6O_{27}$ ceramics

Jun Xiang, Zhan-Guo Liu, Jia-Hu Ouyang*, Fu-Yao Yan

School of Materials Science and Engineering, Harbin Institute of Technology, 92 West Da-Zhi Street, Harbin 150001, China

Received 18 June 2013; received in revised form 1 August 2013; accepted 2 August 2013
Available online 13 August 2013

Abstract

$La_{10}Si_6O_{27}$ ceramics powders were synthesized via the high temperature solid state reaction, and were then pressureless-sintered to obtain dense bulk ceramics by adjusting the sintering parameters. Crystal structure and electrical conductivity of $La_{10}Si_6O_{27}$ ceramics were investigated by X-ray diffraction, scanning electron microscopy, transmission electron microscopy, Raman spectroscopy and complex impedance analysis. $La_{10}Si_6O_{27}$ ceramics obtained at sintering parameters of 1923 K and 10 h has the highest electrical conductivity of 1.28×10^{-2} S cm^{-1} at test temperature of 1073 K. Sintering temperature have a distinct effect on the bulk density of samples and the content of La_2SiO_5 second phase. The content of La_2SiO_5 second phase is inversely proportional to electrical conductivity of as-sintered samples, while the bulk density is directly proportional to electrical conductivity of $La_{10}Si_6O_{27}$ ceramics.

Keywords: B. Microstructure; C. Electrical conductivity; Lanthanum silicate; Oxy-apatite; Sintering temperature

1. Introduction

Oxy-apatite lanthanum silicates are the most attractive candidates for intermediate temperature electrolytes of solid oxide fuel cells (SOFCs) applications due to low operating temperatures of less than 873–1073 K, low activation energy, excellent long-term stability, a wide range of materials selection and relatively low processing cost [1–5]. Recently, many researchers reported high oxide-ionic conductivity of oxy-apatite lanthanum silicates [6–10]. Rather than traditional SOFC electrolytes of fluorite and perovskite structures with the anion-vacancy conduction mechanism, oxy-apatite silicates are novel electrolytes with a conduction mechanism of interstitial oxide-ion migration [11–20].

The crystal structure of lanthanum silicates is hexagonal oxy-apatite structure with a space group *P*63/*m*, which is constituted of covalent and isolated silicate tetrahedra (SiO_4). The La cations are situated at seven-coordinated sites named 6*h* and nine-coordinated sites named 4*f*. In lanthanum silicates, interstitial oxide ions are demonstrated to migrate in the conduction channels along the *c*-axis via a complex sinusoidal pathway, hence the conductivity is much higher parallel to the *c*-axis than perpendicular to this direction [21]. The interstitial oxide ions neighboring the silicate units were well evidenced by nuclear magnetic resonance (NMR) and Raman spectroscopy [22–24].

However, the influence of sintering parameters on structure and electrical conductivity of oxy-apatite lanthanum silicates remains unclear in the open literature. Therefore, in the present work, the crystal structure and electrical conductivity of $La_{10}Si_6O_{27}$ ceramics were investigated by tailoring the sintering parameters.

2. Experimental procedures

$La_{10}Si_6O_{27}$ ceramics were synthesized via the high temperature solid state reaction process. Ultrapure La_2O_3 powder (Grirem Advanced Materials Co. Ltd., Beijing, China; purity $\geq$ 99.9%) and SiO_2 powder (Huijing New Materials Ltd., Shanghai, China; purity $\geq$ 99.9%) were used as original materials. In order to attain complete decarbonation and

*Corresponding author. Tel./fax: +86 451 86414291.
E-mail address: ouyangjh@hit.edu.cn (J.-H. Ouyang).

0272-8842/$ - see front matter © 2013 Elsevier Ltd and Techna Group S.r.l. All rights reserved.
http://dx.doi.org/10.1016/j.ceramint.2013.08.012

dehydroxylation, precalcining of La_2O_3 powder was performed at 1173 K for 2 h before weighing. These powders in appropriate ratios were mechanically ball-milled in analytically pure ethanol for 24 h with zirconia balls at 400 rpm, and were dried at 373 K. These powder mixtures were then calcined at 1623 K for 10 h. The as-calcined powders were uniaxially compacted in a steel mold at 20 MPa, and were then cold isostatically pressed under a pressure of 260 MPa for 8 min. After that, the compacts were pressureless-sintered under the condition of designed sintering parameters as shown in Table 1.

The as-sintered samples were characterized using X-ray diffraction (XRD, Rigaku D/Max-rB, Japan) with monochromatized Cu Kα radiation in a 2θ range of 10–70° at a scanning rate of 4 deg min^{-1}. Surface morphologies of sintered samples were determined by a scanning electron microscope (SEM, Helios Nanolab 600i, USA). The samples were polished and thermally etched at a temperature, which is 50 K lower than the sintering temperature for 30 min. Thermally etched surfaces of samples were covered with a thin gold coating for a better image definition. The bulk densities of all the sintered samples were measured by the Archimedes method with an immersion medium of deionized water. Microstructure of sintered samples was observed by transmission electron microscopy (TEM, FEI Tecnai G2 F30, USA). For TEM observations, the specimens were first ground down to a thickness of 50 μm, and were then prepared by ion beam thinner in argon. Raman spectra were recorded by Raman microscope (LabRAM HR800, Horiba Jobin Yvon, France). The measurement was performed with a 458 nm line of an argon ion laser at room temperature. The laser power was selected to be 20 mW, and the spot diameter was 1 μm. The Raman shift range was from 100 to 1000 cm^{-1}.

The AC impedance/gain-phase analyzer (Solartron™ SI 1260, UK) combined with electrochemical interface (Solartron™ SI 1287, UK) was used to measure the impedance of $La_{10}Si_6O_{27}$ ceramics in air. Platinum pastes were painted on both surfaces of the specimens with a diameter of 8 mm and a thickness of 1 mm as the electrodes, which were heated to 1273 K for 2 h in air in order to adhere to the specimen surfaces. For the measurements of the impedance plots, the specimens were heated from 673 to 1173 K at a heating rate of 5 K min^{-1}. The temperature interval was 50 K and the stabilization time was 15 min between continuous measurements. The measurement frequency was in the range of 20 Hz to 20 MHz and the AC signal strength was 50 mV. The Zview software was used to analyze the results.

Table 1
Sintering parameters of $La_{10}Si_6O_{27}$ ceramics.

Sintering temperature (K)	Sintering time (h)		
1873	5	10	15
1923	5	10	15
1973	5	10	15

3. Results and discussion

3.1. Sintering parameters on microstructures for $La_{10}Si_6O_{27}$ ceramics

XRD patterns of $La_{10}Si_6O_{27}$ ceramics under different sintering conditions are shown in Fig. 1. The main diffraction peaks of all the specimens under different sintering parameters are in agreement with the standard XRD spectrum of $La_{10}(SiO_4)_6O_3$ (JCPDS no. 53-0291), which belongs to hexagonal apatite structure with a space group *P*63/*m*. From Fig. 1, no starting powders are found in sintered samples. However, all the specimens also contain a small amount of second phase La_2SiO_5 (JCPDS no. 40-0234), which belongs to monoclinic structure with a space group *P*21/c. The ionic ratio of La^{3+} to Si^{4+} is 1.67:1 in $La_{10}Si_6O_{27}$ ceramics prepared by high temperature solid state reaction, which is close to 2:1, so it is easy to form the second phase La_2SiO_5.

XRD patterns of $La_{10}Si_6O_{27}$ ceramics sintered at different temperatures for 10 h are shown in Fig. 1(a). With increasing the sintering temperature from 1873 K to 1923 K, the diffraction peaks of $La_{10}Si_6O_{27}$ ceramics are clearly more incisive, while the peaks of La_2SiO_5 second phase are very lower. The higher the sintering temperature, the lower content the second phase La_2SiO_5. However, when the sintering temperature increases to 1973 K, $La_{10}Si_6O_{27}$ ceramics becomes melted completely. In the present work, the melting points of La_2O_3 and amorphous SiO_2 starting powders are 2490 K and 1983 K, respectively. When the sintering temperature is selected at 1923 K, $La_{10}Si_6O_{27}$ ceramics exhibits uniform grains and a lowest content of second phase La_2SiO_5.

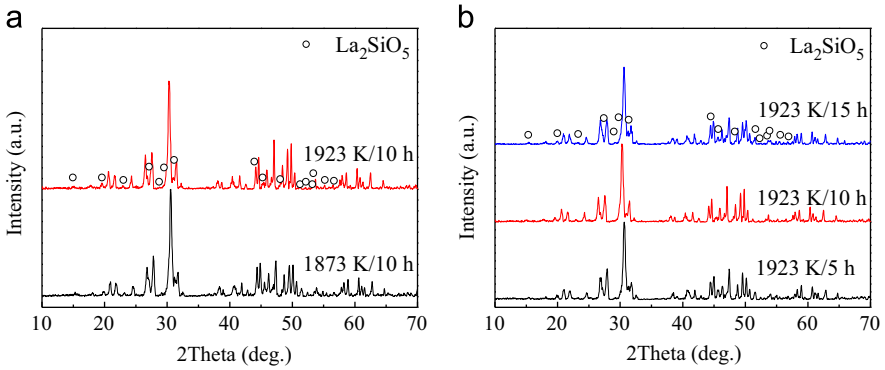

Fig. 1. XRD patterns of $La_{10}Si_6O_{27}$ ceramics under different sintering conditions: (a) different sintering temperatures; and (b) different sintering time.

Fig. 1(b) shows XRD patterns of $La_{10}Si_6O_{27}$ ceramics sintered at 1923 K for different time. When the sintering time is 10 h, $La_{10}Si_6O_{27}$ ceramics exhibits strong diffraction peaks. However, these peaks become broadening when the sintering time is prolonged to 15 h, which may overheat the $La_{10}Si_6O_{27}$ ceramics and result in partial melting. In addition, when the sintering time increases from 5 h to 10 h, the peak intensities of La_2SiO_5 second phase are distinctly reduced.

Microstructures of $La_{10}Si_6O_{27}$ ceramics sintered at different temperatures are shown in Fig. 2. Obviously, the grains grow well on the surfaces of all these specimens, and the grain size is between 3 and 10 μm. The grain boundary is very clean, and the bulk density is quite high. From Fig. 2(a), the grain size is relatively small when the sintering temperature is 1873 K. However, the grain size increases obviously with increasing the sintering temperature to 1923 K (Fig. 2(b)–(d)). Comparing with the microstructures in previous literatures [25–28], we know that the regions pointed by arrows are the partial melting area, which is caused by the use of the amorphous silica as raw powders in this work.

Fig. 3 shows the bulk density of $La_{10}Si_6O_{27}$ ceramics obtained under different sintering conditions. Theoretical density of $La_{10}Si_6O_{27}$ ceramics is 5.614 g cm^{-3} by the criterion PCPDF from XRD. With increasing the sintering temperature, the bulk density of $La_{10}Si_6O_{27}$ ceramics decreases distinctly, as shown in Fig. 3(a). The sintering temperature is one of the most important influencing factors to the densification process. However, too high sintering temperature will result in abnormal growth of grains and partial melting phenomenon easily. When the sintering temperature is 1923 K, and the densification process is almost complete. At 1973 K, $La_{10}Si_6O_{27}$ ceramics is completely melted into the crucible. Therefore, the sintering temperature of $La_{10}Si_6O_{27}$ ceramics is optimized to be 1923 K. Fig. 3(b) shows the bulk density of $La_{10}Si_6O_{27}$ ceramics at 1923 K for different sintering time. Clearly, the bulk density decreases gradually with increasing the sintering time from 5 h to 15 h.

Fig. 4 shows TEM micrographs and the corresponding zone axis selected area electron diffraction (SAED) patterns of $La_{10}Si_6O_{27}$ ceramics sintered at 1923 K for 10 h. From Fig. 4(a), the grain boundary is very clean, and no impurity phase is found at grain boundary. Fig. 4(b)–(d) shows the SAED patterns at different locations of A, B and C as marked in (a), respectively. These patterns indicate that $La_{10}Si_6O_{27}$ ceramics are well crystallized. The SAED pattern of the grain A corresponds to [111] zone axis, with a hexagonal structure of $La_{10}Si_6O_{27}$ ceramics; The SAED patterns of the grains B and C correspond to [100] and $[\bar{2}1\bar{1}]$ zone axis, respectively, with a monoclinic structure of La_2SiO_5. The SAED patterns in Fig. 4(b)–(d) only contain these two crystal lattices of hexagonal $La_{10}Si_6O_{27}$ and monoclinic La_2SiO_5, no other phases are found, which is consistent with the above XRD results.

3.2. Raman analysis of $La_{10}Si_6O_{27}$ ceramics

Fig. 5 shows microstructures and Raman spectra of $La_{10}Si_6O_{27}$ ceramics at different sintering temperatures. Fig. 5(c) corresponds to D, E, and F regions of (a), while Fig. 5(d) corresponds to G, H, and I regions of (b). Microstructures of $La_{10}Si_6O_{27}$ ceramics obtained at different sintering temperatures contain three kinds of different morphologies,

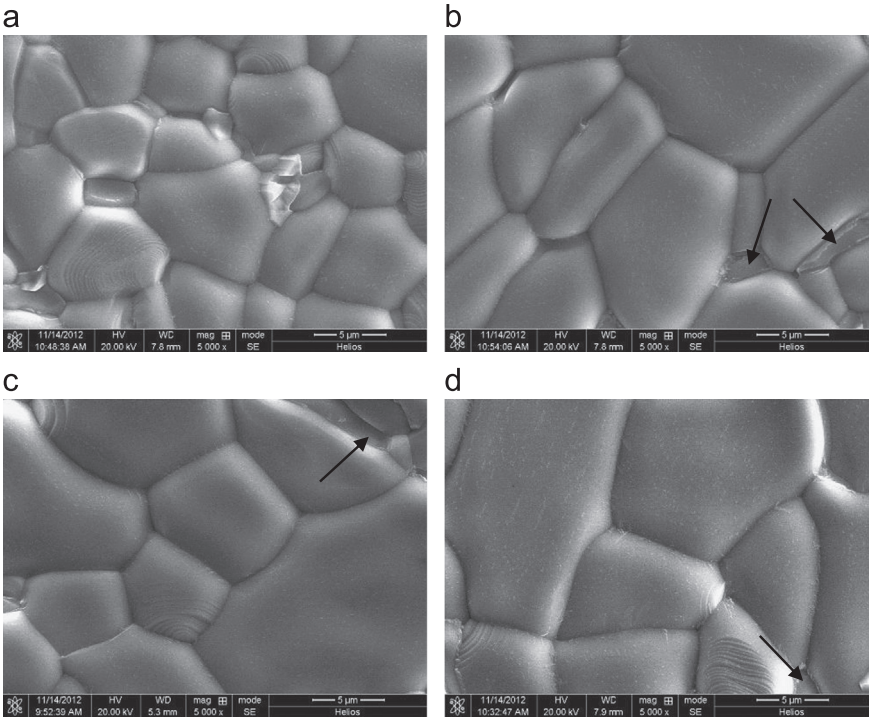

Fig. 2. Microstructures of $La_{10}Si_6O_{27}$ ceramics under different sintering conditions: (a) 1873 K for 10 h; (b) 1923 K for 10 h; (c) 1923 K for 5 h; and (d) 1923 K for 15 h.

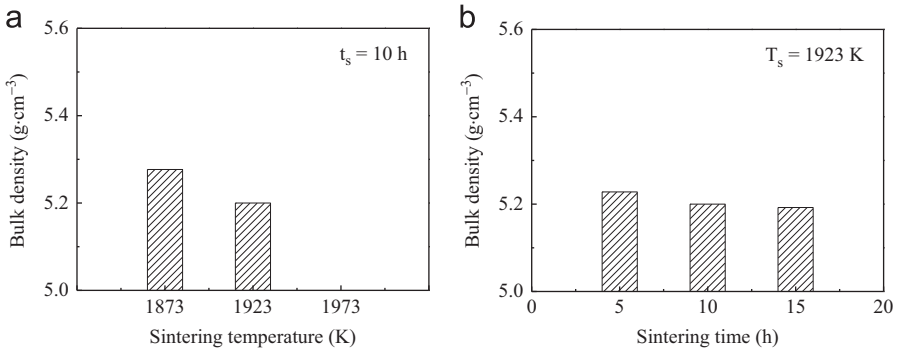

Fig. 3. Bulk density of $La_{10}Si_6O_{27}$ ceramics under different sintering conditions: (a) bulk density *vs*. sintering temperature; and (b) bulk density *vs*. sintering time.

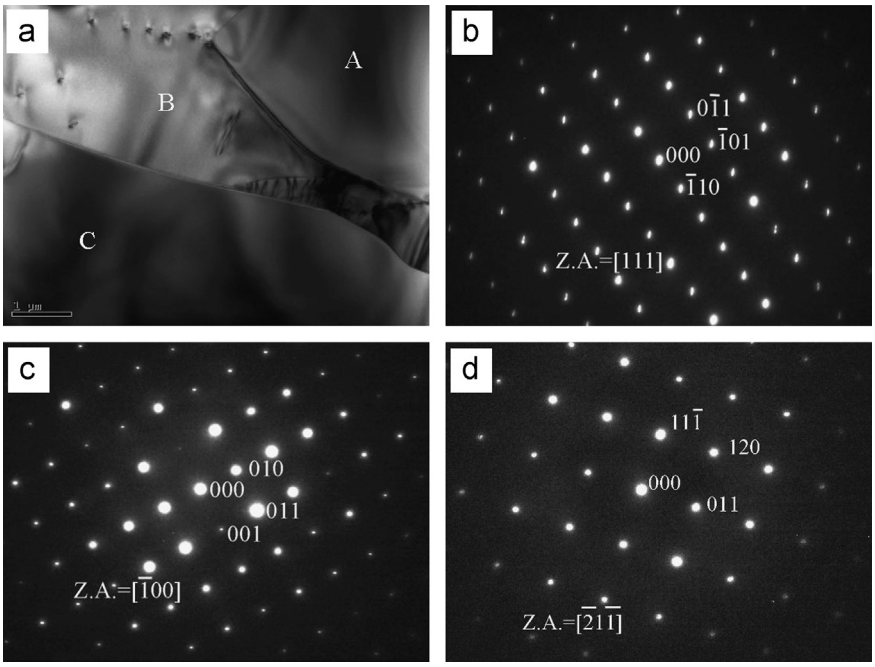

Fig. 4. TEM micrographs and the corresponding zone axis selected area electron diffraction patterns of $La_{10}Si_6O_{27}$ ceramics sintered at 1923 K for 10 h: (a) TEM micrograph of $La_{10}Si_6O_{27}$ ceramics; (b), (c) and (d) selected area electron diffraction patterns at different locations of A, B and C in (a), respectively.

including polygonal, lathy and plicated grains. As shown in Fig. 5(c) and (d), Raman spectra recorded from different spots of each specimen are almost the same, such as band position, band relative intensity and band half-width. In the present work, major bands positions of Raman spectra in the range of 100–1000 cm^{-1} obtained at both sintering temperatures of 1873 K and 1923 K corresponds to those reported in previous studies related to oxy-apatites [29,30]. The integral range can be divided at 350 cm^{-1} into two distinctly different areas. The bands above 350 cm^{-1} can be assigned to internal modes of the pseudo tetrahedral SiO_4 units at frequencies closely related to those of the free species. The band in the range of 370–390 cm^{-1} can be assigned to the symmetric bending mode v_2, the band around 525 cm^{-1} can be due to the asymmetric bending mode v_4, the band at 850 cm^{-1} and 920 cm^{-1} can correspond to the symmetric stretching mode v_1 and asymmetric stretching mode v_3 of SiO_4 tetrahedra. However, the external bands below 350 cm^{-1} can be assigned to translational, vibrational and rotational of the SiO_4 units. Fig. 6 shows the Raman spectra of $La_{10}Si_6O_{27}$ ceramics at different sintering temperatures. With increasing the sintering temperature from 1873 K to 1923 K, some weak bands become weakening or annihilate, in the meantime the half-width of bands are magnified. It indicates that with increasing the sintering temperature from 1873 K to 1923 K, partial melting occurs on the surface of $La_{10}Si_6O_{27}$ ceramics, which causes the increase in the short range disorder degree of structure. As these weak bands correspond to the characteristic peaks of second phase La_2SiO_5, increasing the sintering temperature will decrease the content of second phase La_2SiO_5.

The stretching modes of Raman spectra are particularly sensitive to the neighboring disorders, such as atoms from other sub-lattices or electric defects resulting from substitutions/vacancies, whereas the symmetric bending modes are specifically susceptible to local geometric disorientation. Therefore, the changes in symmetric

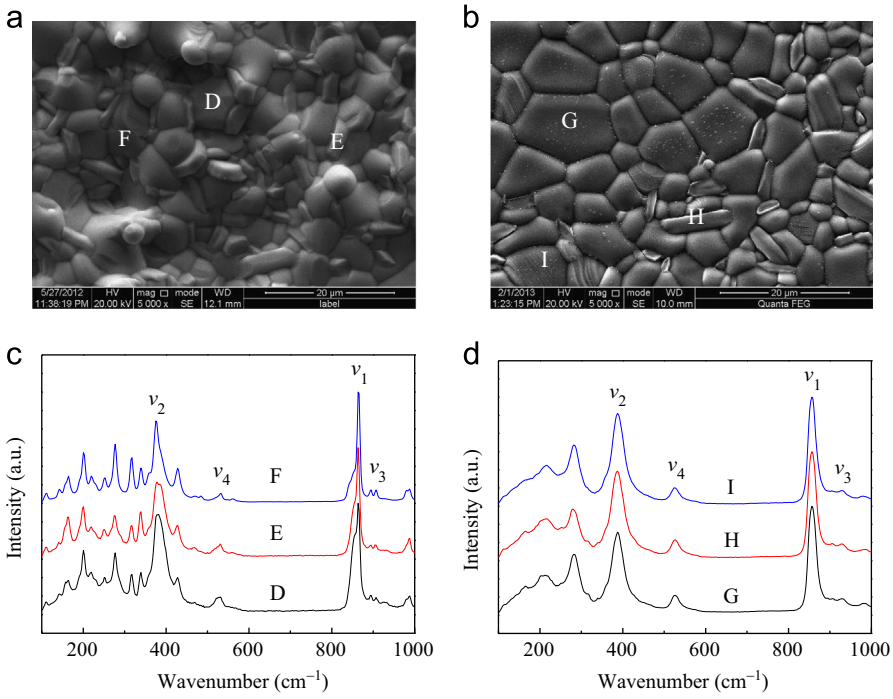

Fig. 5. Microstructures and Raman spectra of $La_{10}Si_6O_{27}$ ceramics at different sintering temperatures: (a) microstructures of $La_{10}Si_6O_{27}$ ceramics sintered at 1873 K; (b) microstructures of $La_{10}Si_6O_{27}$ ceramics sintered at 1923 K; (c) Raman spectra of D, E and F in (a); and (d) Raman spectra of G, H and I in (b).

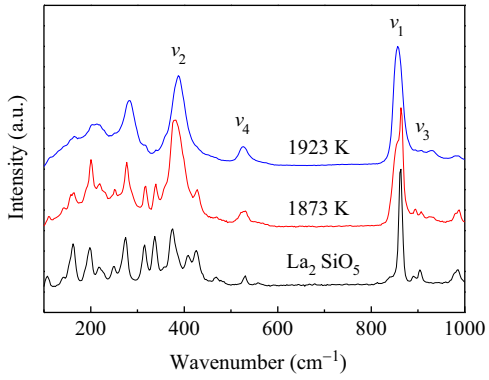

Fig. 6. Raman spectra of $La_{10}Si_6O_{27}$ and La_2SiO_5 ceramics sintered at different temperatures.

stretching mode v_1 will be able to distinguish the neighboring disorders of oxygen ions defects, which are responsible for electrical conductivity of $La_{10}Si_6O_{27}$ ceramics prepared under different sintering conditions. Fig. 7 shows the decomposition of the symmetric stretching mode v_1 of SiO_4 tetrahedral into Lorentzian components for $La_{10}Si_6O_{27}$ ceramics under different sintering conditions. As shown in Fig. 7(a) and (b), the symmetric stretching mode v_1 can be decomposed into three main bands at 849.12 cm^{-1}, 856.55 cm^{-1}, 864.67 cm^{-1} and 849.62 cm^{-1}, 855.63 cm^{-1}, 862.7 cm^{-1}, respectively, which is similar to previous results reported in related literatures [31]. However, the band centered at 862.7 cm^{-1} is obviously broadened. This indicates that the disorder degree of structure increases with increasing the sintering temperature from 1873 K to 1923 K. Fig. 8 shows the decomposition of the symmetric bending mode v_2 of SiO_4 tetrahedral into Lorentzian components for $La_{10}Si_6O_{27}$ ceramics under different sintering conditions. An additional band shoulder at 360 cm^{-1} is found in the oxygen-excessive $La_{8+x}Sr_{2-x}(SiO_4)_6O_{2+x/2}$ samples with its intensity increasing with increasing x [32]. As shown in Fig. 8(a) and (b), the fourth band at around 360 cm^{-1} can be found, all the samples of $La_{10}Si_6O_{27}$ under different sintering temperatures are oxygen-excessive in the present work. In addition, as the intensity of the fourth band in Fig. 8(b) is higher than that in Fig. 8(a), the specimen contains more interstitial oxygen with increasing the sintering temperature from 1873 K to 1923 K.

3.3. Electrical responses of as-synthesized oxide ceramics

Fig. 9 shows the impedance plots at 673 K and corresponding equivalent circuit of $La_{10}Si_6O_{27}$ ceramics under different sintering conditions. From Fig. 9, all the AC impedance spectra are composed of two interconnected semicircular arcs and an incomplete semicircular. The fitting parameters of grain resistance (R_g), grain boundary resistance (R_{gb}), grain capacitance (CPE_g) and grain boundary capacitance (CPE_{gb}) for $La_{10}Si_6O_{27}$ ceramics under different sintering conditions are all acquired by Zview software (Table 2). The ranges of capacitances are from 1.89×10^{-11} to 7.61×10^{-10} F cm^{-1} in the high frequency, and from 6.79×10^{-8} to 1.16×10^{-7} F cm^{-1} in the medium frequency. These two semicircular arcs correspond to the grain impedance and the grain boundary impedance process, respectively. However, the incomplete semicircular represents the electrode interface diffusion, which is the representative of Wagner ionic diffusion effect. The electrolyte of oxy-apatite type $La_{10}Si_6O_{27}$ ceramics is predominantly conducted by ionic

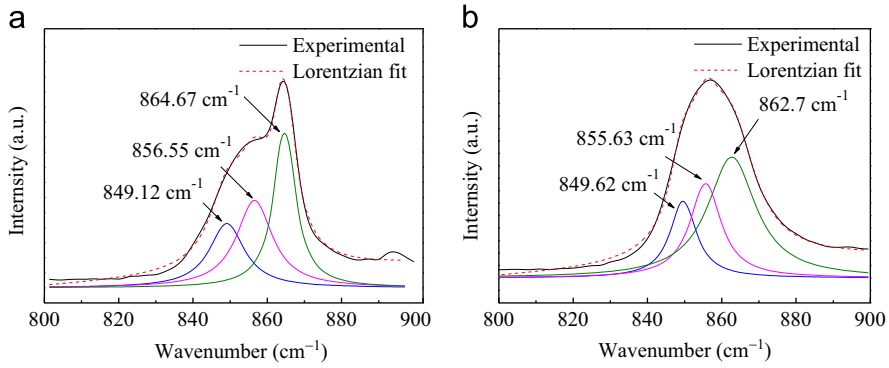

Fig. 7. Decomposition of the symmetric stretching mode v_1 of SiO_4 tetrahedral into Lorentzian components for $La_{10}Si_6O_{27}$ ceramics under different sintering conditions: (a) 1873 K for 10 h; and (b) 1923 K for 10 h.

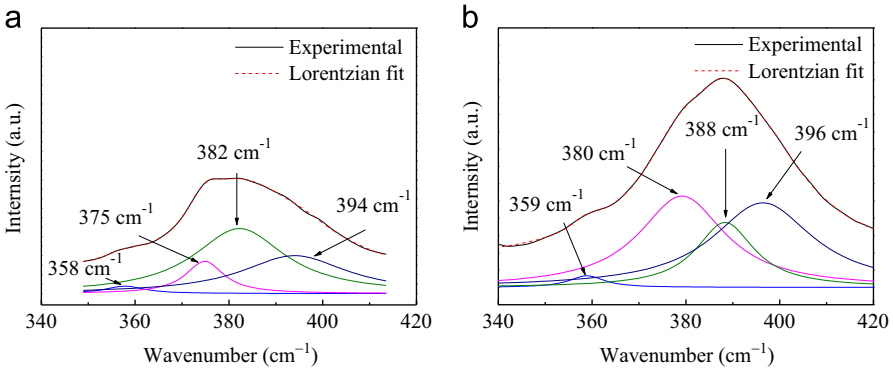

Fig. 8. Decomposition of the symmetric bending mode v_2 of SiO_4 tetrahedral into Lorentzian components for $La_{10}Si_6O_{27}$ ceramics under different sintering conditions: (a) 1873 K for 10 h; and (b) 1923 K for 10 h.

carriers. From Fig. 9(a) and (b), all the semicircular arcs corresponding to the grain impedance and the grain boundary impedance decrease clearly with increasing the sintering temperature from 1873 K to 1923 K, even more for the semicircular arcs correspond to the grain boundary impedance. That is because the cavities within materials are eliminated following the rise of sintering temperature, which is beneficial for grain to grow up. If the size of grain is big, the amount of grain boundary is less for certain bulk specimens. This is concordant with the SEM results in Fig. 2. The big size grains and little amount grain boundaries are all helpful to conducting the interstitial oxygen ions, consequently, the grain impedance and the grain boundary impedance have decreased. It indicates that the grain size plays an important role in the grain impedance of $La_{10}Si_6O_{27}$ ceramics. Fig. 9(b)–(d) shows the AC impedance spectra at 1923 K for different sintering time. The semicircular arc corresponding to the grain impedance has no significant change with the sintering time. When the sintering temperature remains unchanged, the grain size has a little change. However, the semicircular arc corresponding to the grain boundary impedance inclines to decrease firstly and then increase. The second phase La_2SiO_5 is usually situated at the grain boundaries of $La_{10}Si_6O_{27}$ ceramics, and exhibits a negative effect on the conduction of interstitial oxygen ion. Therefore, the grain boundary impedance decreases evidently with decreasing the content of second phase La_2SiO_5. When the sintering time is prolonged from 10 h to 15 h at 1923 K, the content of second phase La_2SiO_5 has almost no change, however the grain boundary impedance increases slightly. As we all know, the grain size usually has an important effect on the macroscopic properties [33], so the importance of the grain size should be considered for electrical properties. The grain and grain boundary conductivity of $La_{10}Si_6O_{27}$ ceramics at 673 K under different sintering conditions are shown in Table 3. It can be seen from Table 3 that the grain conductivity of $La_{10}Si_6O_{27}$ ceramics sintered at 1923 K for different sintering time are all an order of magnitude higher than that of $La_{10}Si_6O_{27}$ ceramics sintered at 1873 K, which indicates that the higher sintering temperature, the bigger grain size, and the higher grain conductivity. In addition, the grain boundary amount at 1923 K is more than that at 1873 K, so the grain boundary conductivity is little higher than that at 1873 K.

Fig. 10 shows the AC impedance plots in the temperature range of 673–1173 K in air and corresponding equivalent circuit of $La_{10}Si_6O_{27}$ ceramics sintered at 1923 K for 10 h. Clearly, with increasing the measurement temperature, the semicircular arcs corresponding to the grain and grain boundary impedance decrease evidently and shift to the high frequency. At 873 K, the semicircular arcs corresponding to the grain impedance disappear. In addition, the ray representing electrode interface diffusion becomes to bend down gradually, and then forms a distinct semicircular arc. The transport ability of interstitial oxygen ion increases with increasing the measurement temperature. As the polarization process accelerates, the polarization relaxation time becomes shortened. The polarization relaxation frequencies of both

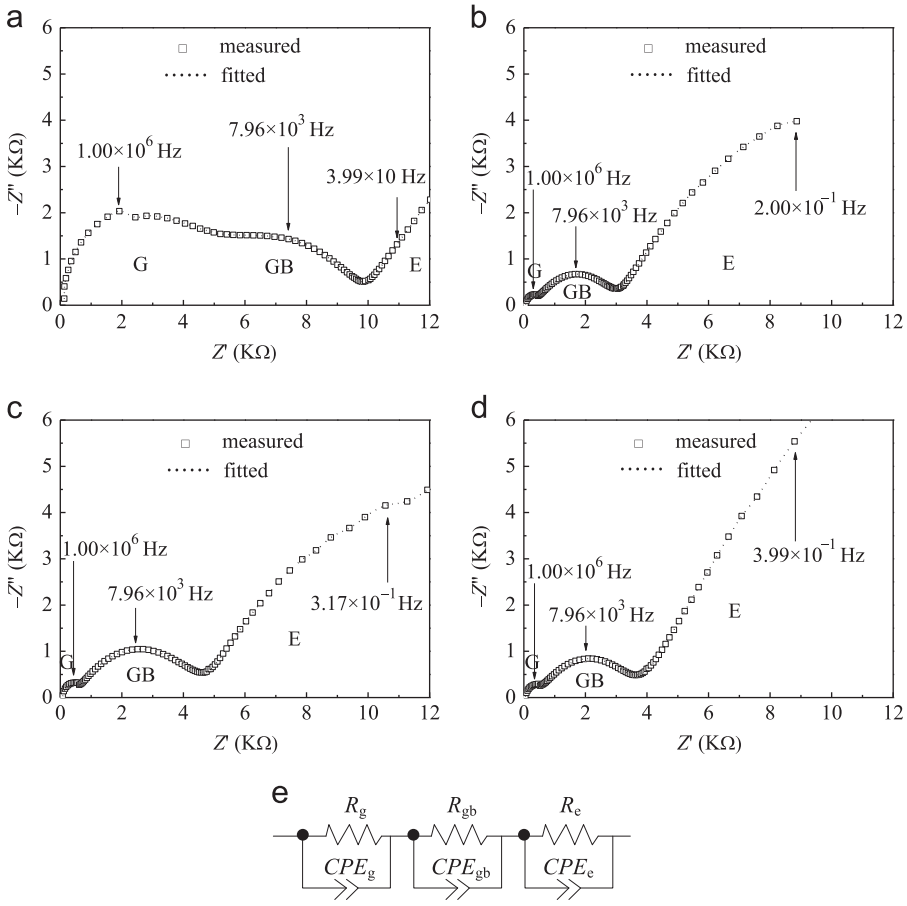

Fig. 9. Impedance plots at test temperature of 673 K and corresponding equivalent circuit of $La_{10}Si_6O_{27}$ ceramics under different sintering conditions: (a) 1873 K for 10 h; (b) 1923 K for 10 h; (c) 1923 K for 5 h; (d) 1923 K for 15 h; and (e) equivalent circuit.

Table 2
Fitting parameters of grain resistance (R_g), grain boundary resistance (R_{gb}), grain capacitance (CPE_g) and grain boundary capacitance (CPE_{gb}) at 673 K for $La_{10}Si_6O_{27}$ ceramics under different sintering conditions.

Sintering parameters	R_g (Ω)	R_{gb} (Ω)	CPE_g (F cm^{-1})	CPE_{gb} (F cm^{-1})
1873 K for 10 h	3213	6696	1.89×10^{-11}	6.79×10^{-8}
1923 K for 10 h	416.4	2583	7.61×10^{-10}	1.16×10^{-7}
1923 K for 5 h	528.4	4029	1.83×10^{-10}	8.15×10^{-8}
1923 K for 15 h	511.8	3116	6.31×10^{-10}	9.48×10^{-8}

Table 3
The conductivity of grain and grain boundary at 673 K for $La_{10}Si_6O_{27}$ ceramics under different sintering conditions.

Sintering parameters	σ_g (S cm^{-1})	σ_{gb} (S cm^{-1})
1873 K for 10 h	6.46×10^{-5}	3.10×10^{-5}
1923 K for 10 h	4.86×10^{-4}	7.83×10^{-5}
1923 K for 5 h	3.88×10^{-4}	5.09×10^{-5}
1923 K for 15 h	4.14×10^{-4}	6.80×10^{-5}

grain and grain boundary shift to a high frequency, and finally beyond the upper limit (20 MHz) of measurement frequency. Nevertheless, both grain and grain boundary resistances will decrease with increasing the measurement temperature. At 873 K, the semicircular arcs corresponding to the grain impedance disappear, and the grain capacitance can be neglected. Therefore, the two semicircular arcs correspond to the grain boundary impedance and electrode interface diffusion process. It is concluded that the grain impedance will disappear with increasing the measurement temperature, while the grain boundary impedance is available and decrease gradually.

Arrhenius plots of total conductivity of $La_{10}Si_6O_{27}$ ceramics at different sintering temperatures are presented in Fig. 11(a). Clearly, the measured total conductivity at 1923 K is an order of magnitude higher than that at 1873 K. In combination with XRD results, increasing the sintering temperature will decrease the content of second phase La_2SiO_5 remarkably. The higher the sintering temperature, the lower the content of second phase La_2SiO_5, the

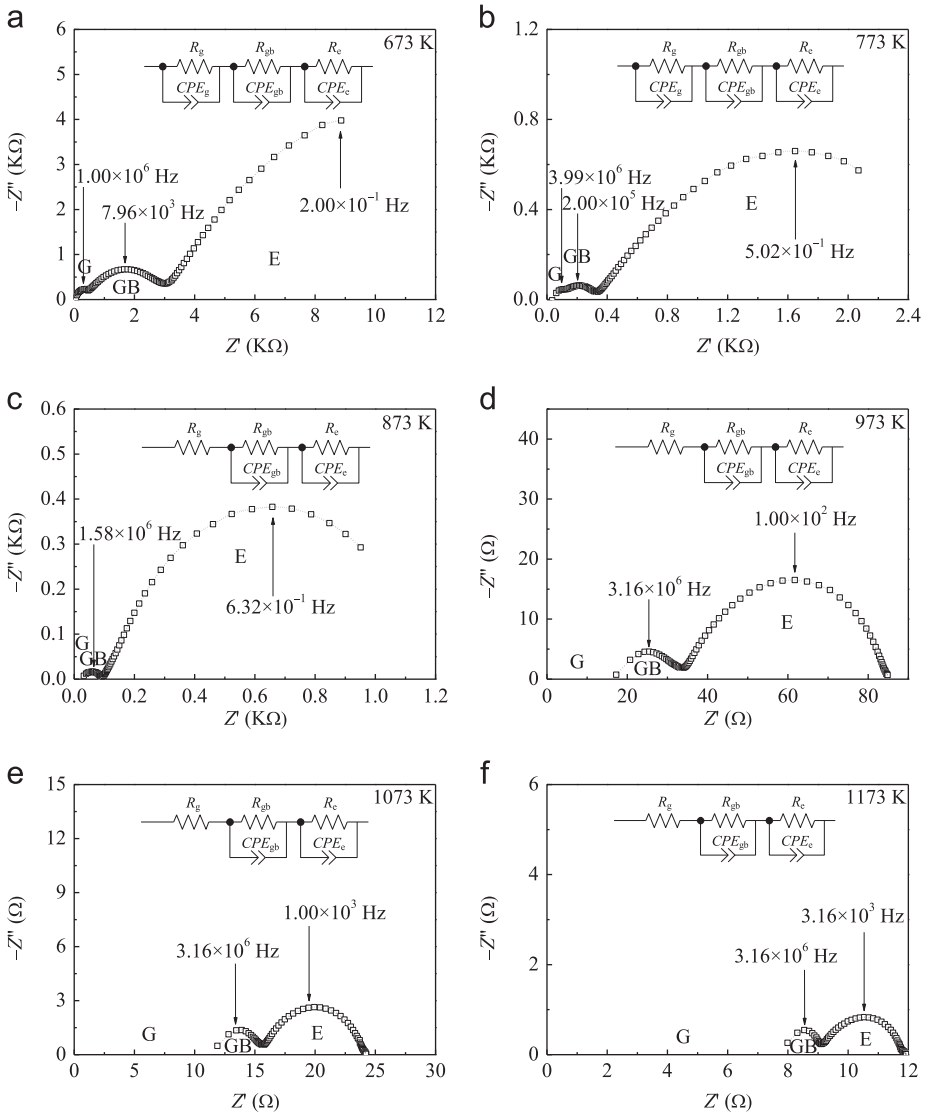

Fig. 10. Impedance plots at different test temperatures and corresponding equivalent circuit of $La_{10}Si_6O_{27}$ ceramics sintered at 1923 K for 10 h: (a) 673 K; (b) 773 K; (c) 873 K; (d) 973 K; (e) 1073 K; and (f) 1173 K.

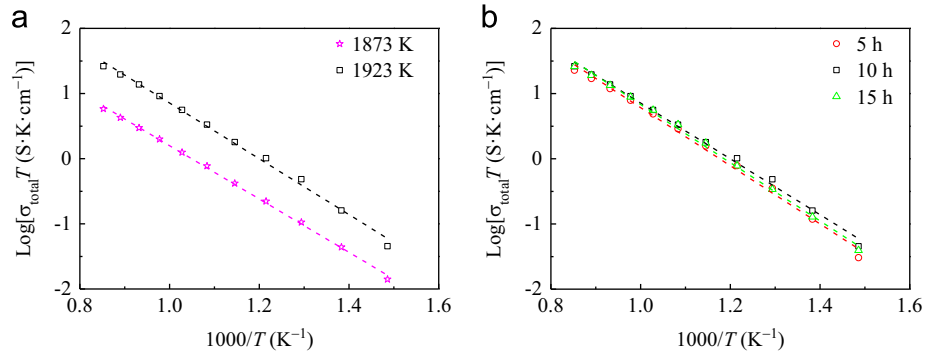

Fig. 11. Arrhenius plots of total conductivity of $La_{10}Si_6O_{27}$ ceramics: (a) at different sintering temperatures for 10 h; and (b) at 1923 K for different sintering time.

higher the total conductivity. Therefore, the content of second phase La_2SiO_5 is the dominated influencing factor of total conductivity. At 1073 K, the highest electrical conductivity of $La_{10}Si_6O_{27}$ ceramics sintered at 1923 K for 10 h reaches 1.28×10^{-2} S cm^{-1}, which is higher than that of the sample prepared by a water-based gel-casting route, and is approximate with the sample prepared by freeze-drying method, tape casting combined with reaction sintering under identical conditions

[29,34,35]. Arrhenius plots of total conductivity of $La_{10}Si_6O_{27}$ ceramics at 1923 K for different sintering time are presented in Fig. 11(b). The total conductivity first increases evidently with prolonging the sintering time from 5 h to 10 h, and then drops slightly up to 15 h. The content of second phase La_2SiO_5 has almost no change when the sintering time is prolonged from 10 h to 15 h, however, the total conductivity still decreases slightly, which may be due to the decrease in the bulk density.

4. Conclusions

(1) Oxy-apatite $La_{10}Si_6O_{27}$ ceramics were prepared via high temperature solid state reaction and subsequent pressureless pressing. The sintering parameters are optimized to be 1923 K and 10 h to get a high purity of $La_{10}Si_6O_{27}$ ceramics.
(2) Sintering parameters have a distinct influence on both the content of second phase La_2SiO_5 and the bulk density of $La_{10}Si_6O_{27}$ ceramics. With increasing the sintering temperature, the content of second phase La_2SiO_5 and the bulk density of $La_{10}Si_6O_{27}$ ceramics decrease obviously. With prolonging the sintering time, the content of second phase La_2SiO_5 decreases first and then remains unchanged, however, the bulk density of $La_{10}Si_6O_{27}$ ceramics decreases monotonously.
(3) The content of second phase La_2SiO_5 is inversely proportional to total conductivity of $La_{10}Si_6O_{27}$ ceramics, which is the dominated influencing factor of total conductivity. The bulk density is directly proportional to total conductivity of $La_{10}Si_6O_{27}$ ceramics.
(4) The content of second phase La_2SiO_5 has a certain influence on the grain size of $La_{10}Si_6O_{27}$. The second phase distributes mainly at the grain boundaries, which blocks the grain growth of $La_{10}Si_6O_{27}$. However, the grain size and grain boundary amount have a distinct influence on total conductivity of $La_{10}Si_6O_{27}$ ceramics. The grain resistance decreases with increasing the grain size, while the grain boundary resistance increases with increasing the grain boundary amount.

Acknowledgments

This work was financially supported by the National Natural Science Foundation of China (NSFC, Grant nos. 51021002 and 51272054), and the Fundamental Research Funds for the Central Universities (Grant no. HIT.BRET1.2010006).

References

[1] A. Orera, T. Baikie, E. Kendrick, J.F. Shin, S. Pramana, R. Smith, T.J. White, M.L. Sanjuan, P.R. Slater, Apatite germanates doped with tungsten: synthesis, structure, and conductivity, Dalton Transactions 40 (2011) 3903–3908.
[2] M. Santos, C. Alves, F.A.C. Oliveira, T. Marcelo, J. Mascarenhas, A. Cavaleiro, B. Trindade, Novel two-step processing route combining mechanical alloying and microwave hybrid sintering to fabricate dense $La_{9.33}Si_2Ge_4O_{26}$ for SOFCs, Journal of Power Sources 231 (2013) 146–152.
[3] S.M. Hosseini, T. Shvareva, A. Navrotsky, Energetics of lanthanum silicate apatite: influence of interstitial oxygen and cation vacancy concentrations in $La_{9.33+x}(SiO_4)_6O_{2+3x/2}$ and $La_{10-x}Sr_x(SiO_4)_6O_{3-0.5x}$, Solid State Ionics 233 (2013) 62–66.
[4] S. Nakayama, A. Ikesue, Y. Higuchi, M. Sugawara, M. Sakamoto, Growth of single-crystals of apatite-type oxide ionic conductor from sintered ceramics by a seeding method, Journal of the European Ceramic Society 33 (2013) 207–210.
[5] F. Sun, N.N. Zhang, J.L. Li, H.L. Liao, Preparation of dense silicate electrolyte coating with low pressure plasma spraying and very low pressure plasma spraying for intermediate-temperature solid oxide fuel cells, Journal of Power Sources 223 (2013) 36–41.
[6] L. Leon-Reina, J.M. Porras-Vazquez, E.R. Losilla, D.V. Sheptyakov, A. Llobet, M.A.G. Aranda, Low temperature crystal structures of apatite oxygen–conductors containing interstitial oxygen, Dalton Transactions (20) (2007) 2058–2064.
[7] A. Mineshige, T. Nakao, M. Kobune, T. Yazawa, H. Yoshioka, Electrical properties of $La_{10}Si_6O_{27}$-based oxides, Solid State Ionics 179 (2008) 1009–1012.
[8] S. Nakayama, M. Sakamoto, M. Higuchi, K. Kodaira, M. Sato, S. Kakita, T. Suzuki, K. Itoh, Oxide ionic conductivity of apatite type $Nd_{9.33}(SiO_4)_6O_2$ single crystal, Journal of the European Ceramic Society 19 (1999) 507–510.
[9] A. Orera, P.R. Slater, Water incorporation studies in apatite-type rare earth silicates/germinates, Solid State Ionics 181 (2010) 110–114.
[10] J.E.H. Sansom, P.A. Sermon, P.R. Slater, Synthesis and conductivities of the Ti doped apatite-type phases $(La/Ba)_{10-x}(Si/Ge)_{6-y}Ti_yO_{26+z}$, Solid State Ionics 176 (2005) 1765–1768.
[11] M. Karlsson, Perspectives of neutron scattering on proton conducting oxides, Dalton Transactions 42 (2013) 317–329.
[12] V. Oygarden, T. Grande, Crystal structure, electrical conductivity and thermal expansion of Ni co-doped $LaCoO_3$, Dalton Transactions 42 (2013) 2704–2715.
[13] Y.H. Chou, N. Hondow, C.I. Thomas, R. Mitchell, R. Brydson, R.E. Douthwaite, Microwave plasma synthesis of lanthanide zirconates from microwave transparent oxides, Dalton Transactions 41 (2013) 2472–2476.
[14] Y. Ledemi, M. El Amraoui, J.L. Ferrari, P.L. Fortin, S.J.L. Ribeiro, Y. Messaddeq, Infrared to visible up-conversion emission in Er^{3+}/Yb^{3+} codoped fluoro-phosphate glass–ceramics, Journal of the American Ceramic Society 96 (2013) 825–832.
[15] T. Ivas, E. Povoden-Karadeniz, N. Grundy, E. Jud-Sierra, J. Grasslin, L.J. Gauckler, Experimental phase diagram determination and thermodynamic assessment of the CeO_2–Ga_2O_3–CoO system, Journal of the American Ceramic Society 96 (2013) 613–626.
[16] X.-L. Xia, J.-H. Ouyang, Z.-G. Liu, The influence of CaO on structure and electrical conductivity of pyrochlore-type $Sm_2Zr_2O_7$, Journal of Power Sources 189 (2009) 888–893.
[17] Z.-G. Liu, J.-H. Ouyang, K.-N. Sun, X.-L. Xia, Effect of Gd and Yb co-doping on structure and electrical conductivity of the $Sm_2Zr_2O_7$ pyrochlore, Journal of Power Sources 195 (2010) 7225–7229.
[18] X.-L. Xia, J.-H. Ouyang, Z.-G. Liu, Electrical properties of gadolinium–europium zirconate ceramics, Journal of the American Ceramic Society 93 (2010) 1074–1080.
[19] L.P. Li, J.C. Nino, Ionic conductivity across the disorder–order phase transition in the $SmO_{1.5}$–CeO_2 system, Journal of the European Ceramic Society 32 (2012) 3543–3550.
[20] V. Sariboga, H. Ozdemir, M.A.F. Oksuzomer, Cellulose templating method for the preparation of $La_{0.8}Sr_{0.2}Ga_{0.83}Mg_{0.17}O_{2.815}$ (LSGM) solid oxide electrolyte, Journal of the European Ceramic Society 33 (2013) 1435–1446.
[21] K. Fukuda, T. Asaka, M. Oyabu, D. Urushihara, A. Berghout, E. Bechade, O. Masson, I. Julien, P. Thomas, Crystal structure and oxide-ion conductivity along *c*-axis of apatite-type lanthanum silicate with excess oxide ions, Chemistry of Materials 24 (2012) 4623–4631.
[22] J.R. Tolchard, M.S. Islam, P.R. Slater, Defect chemistry and oxygen ion migration in the apatite-type materials $La_{9.33}Si_6O_{26}$ and $La_8Sr_2Si_6O_{26}$, Journal of Materials Chemistry 13 (2003) 1956–1961.
[23] J.E.H. Sansom, J.R. Tolchard, D. Apperley, M.S. Islam, P.R. Slater, Solid state ^{29}Si NMR studies of apatite-type oxide-ion conductors, Journal of Materials Chemistry 16 (2006) 1410–1413.

[24] E. Kendrick, M.S. Islam, P.R. Slater, Developing apatites for solid oxide fuel cells: insight into structural, transport and doping properties, Journal of Materials Chemistry 17 (2007) 3104–3111.

[25] H. Azzouz, R. Alouani, S. Tlig, Mineralogical characterization of ceramic tiles prepared by a mixture of cretaceous and mio-pliocene clays from tunisia: factory and laboratory products, Journal of the Ceramic Society of Japan 119 (2011) 93–100.

[26] M.Z. Shoushtari, A. Bahrami, M. Farbod, The effect of silver doping on the critical current density of Bi–Pb–Sr–Ca–Cu–O ceramic superconductor, Physica Status Solidi C 3 (2006) 2994–2998.

[27] T.G.N. Babu, J. Koshy, Development and dielectric properties of $Ba_{2-x}Sr_xDyTaO_6$ ($x=0$, 1, and 2) substrates for $YBa_2Cu_3O_{7-\delta}$ films, Journal of Solid State Chemistry 133 (1997) 522–528.

[28] B.K. Roul, Magnetic and transport critical current density of laser-irradiated Sm–Ba–Cu–O superconductor at 4.2 K, Journal of Superconductivity 6 (1993) 93–98.

[29] L. Zhang, Q.H. Hong, H.W. Wu, C.Z. Li, S.P. Jiang, Synthesis and characterization of doped $La_9ASi_6O_{26.5}$ ($A=$Ca, Sr, Ba) oxyapatite electrolyte by a water-based gel-casting route, International Journal of Hydrogen Energy 36 (2011) 6862–6874.

[30] G. Lucazeau, N. Sergent, T. Pagnier, A. Shaula, V. Kharton, F.M. B. Marques, Raman spectra of apatites: $La_{10-x}Si_{6-y}(Al, Fe)_yO_{26\pm\delta}$, Journal of Raman Spectroscopy 38 (2007) 21–33.

[31] S.H. Jo, P. Muralidharan, D.K. Kim, Raman and ^{29}Si NMR spectroscopic characterization of lanthanum silicate electrolytes: emphasis on sintering temperature to enhance the oxide-ion conductivity, Electrochimica Acta 54 (2009) 7495–7501.

[32] A. Orera, E. Kendrick, D.C. Apperley, V.M. Orera, P.R. Slater, Effect of oxygen content on the ^{29}Si NMR, Raman spectra and oxide ion conductivity of the apatite series, $La_{8+x}Sr_{2-x}(SiO_4)_6O_{2+x/2}$, Dalton Transactions (39) (2008) 5296–5301.

[33] C.H. Lee, H.C. Liu, H.H. Lu, T. Goto, R. Tu, C.A. Wang, S. Pavol, J.L. Ruan, P.K. Nayak, J.H. Chen, Q.Y. Chen, J.L. Huang, Indentation deformation and microcracking in β-Si_3N_4-based nanoceramic, Journal of the American Ceramic Society 95 (2012) 1421–1428.

[34] A. Chesnaud, G. Dezanneau, C. Estournès, C. Bogicevic, F. Karolak, S. Geiger, G. Geneste, Influence of synthesis route and composition on electrical properties of $La_{9.33+x}Si_6O_{26+3x/2}$ oxy-apatite compounds, Solid State Ionics 179 (2008) 1929–1939.

[35] I. Santacruz, J.M. Porras-Vázquez, E.R. Losilla, M.A.G. Aranda, Preparation of aluminium lanthanum oxyapatite tapes, $La_{10}AlSi_5O_{26.5}$, by tape casting and reaction sintering, Journal of the European Ceramic Society 31 (2011) 1573–1580.